

Dispersion broadening of the two-photon quantum interference width due to temporal filtering

Zhiguang Xia^{1,2}, Xiao Xiang¹, Runai Quan,¹ Ruifang Dong^{1,2,*}, Tao Liu,^{1,2,†} and Shougang Zhang^{1,2}

¹Key Laboratory of Time and Frequency Primary Standards, National Time Service Center, Chinese Academy of Sciences, Xi'an, 710600 Shaanxi, China

²School of Astronomy and Space Science, University of Chinese Academy of Sciences, 100049 Beijing, China

(Received 17 April 2023; revised 10 August 2023; accepted 9 October 2023; published 31 October 2023)

Temporal filtering is widely recognized as an effective strategy for improving the visibility of the Hong-Ou-Mandel interferometer, an important tool for observing the phenomenon of two-photon quantum interference. However, such manipulation may lead to additional effects on the measurement. In addition to demonstrating the degradation of photon-detection efficiency, this paper demonstrates that temporal filtering can significantly broaden the interference width, especially in scenarios where photons experience substantial dispersion. This broadening effect is also presented in the nonlocal Franson interferometer. The good agreement between experimental results and theoretical simulations not only reveals the mechanism behind dispersion-induced broadening in two-photon quantum interference but also provides an alternative and convenient method for measuring dispersion without the need for extra equipment.

DOI: 10.1103/PhysRevApplied.20.044080

I. INTRODUCTION

As a representative tool of two-photon quantum interference, the Hong-Ou-Mandel (HOM) interferometer [1] has been extensively studied for its crucial role in modern quantum mechanics [2,3] and versatile applications in quantum information science and technology [4–15]. To broaden the scope of quantum interference applications from local to nonlocal scenarios, the Franson interferometer (FI) was proposed as well [16]. In contrast to the HOM interferometer (HOMI), where a photon pair interferes with itself, the Franson interferometer involves the interference of a photon pair generated at one time with another (identical) photon pair generated at a later time. Based on the Franson interferometer, the HOM-type interference fringe can be observed without use of a common beam splitter [17,18]. Both the visibility and the width of these quantum interferences are important references for characterizing the correlated or entangled nature of the two-photon state and assessing the performance of relevant applications. For example, measurement of the HOM visibility is invaluable for diagnosing the indistinguishability of the single-photon sources and states [19]. Franson interference visibility, on the other hand, characterizes the quality of energy-time entangled photons

[20,21]. Therefore, effective enhancement of visibility in both HOM and Franson interference is of great importance. It has been reported that temporal filtering can significantly increase interference visibility [22,23]. However, there is an additional effect on two-photon quantum interference measurements besides the degradation of measurement efficiency.

In this paper, we demonstrate both in theory and in experiments the mechanism of dispersion-induced broadening in two-photon quantum interference width due to temporal filtering, which is contradictory to the previous cognition of the dispersion cancellation effect in two-photon interferometers [24–26]. Since it is requisite to propagate photon pairs through long-distance fibers for fiber-based quantum information applications [23,27,28], this effect deserves to be characterized. In the following sections, we present a theoretical model for both the HOM interference width and the Franson interference width as functions of the temporal filtering width and the dispersion experienced by energy-time entangled biphotons. Experimental verification is achieved by use of photon pairs generated via the type-II spontaneous parametric down-conversion (SPDC) process by a quasimonochromatic pump to pass through the dispersive media in front of the interferometer. The good agreement between theory and experiments well quantifies the mechanism of dispersion-induced broadening of the quantum interference width under the temporal filtering effect. Furthermore,

*dongruifang@ntsc.ac.cn

†taoliu@ntsc.ac.cn

it provides an alternative and convenient method of evaluating the path dispersion by simply applying temporal filtering to the interference measurements without the need for additional equipment.

II. THEORETICAL DIAGRAM

Schematic diagrams of the HOMI and the FI with dispersive media in the photon paths are shown in Figs. 1(a) and 1(b), respectively. For the HOMI setup, under the condition of temporal filtering of the coincidence window, the photon coincidence rate ($P_{c,\text{HOMI}}$) detected by the photodetectors D_1 and D_2 at the output of the interferometer can be written as

$$P_{c,\text{HOMI}} \propto \int dt_1 \int dt_2 H(t_1 - t_2) \times \langle \Psi_{\text{in}} | \hat{a}_1^+(t_1) \hat{a}_2^+(t_2) \hat{a}_2(t_2) \hat{a}_1(t_1) | \Psi_{\text{in}} \rangle, \quad (1)$$

where $H(t_1 - t_2)$ denotes the temporal filtering function of the coincidence window. For deduction simplicity, a Gaussian function is assumed, i.e., $H(t_1 - t_2) = e^{-(t_1 - t_2)^2/2\tau^2}$. Its corresponding full width at half maximum (FWHM) is given by $2\sqrt{2 \ln 2}\tau$. $|\Psi_{\text{in}}\rangle$ is the two-photon state function in the time domain. $\hat{a}_j^+(t_j)$, $j = 1, 2$, represents the annihilation (creation) operator of the single photon arriving at the j th detector at time t_j , and its Fourier transformation in the frequency domain can be given by

$$\hat{a}_j(t_j) \propto \int d\omega \hat{a}_j(\omega) e^{-i\omega t_j}. \quad (2)$$

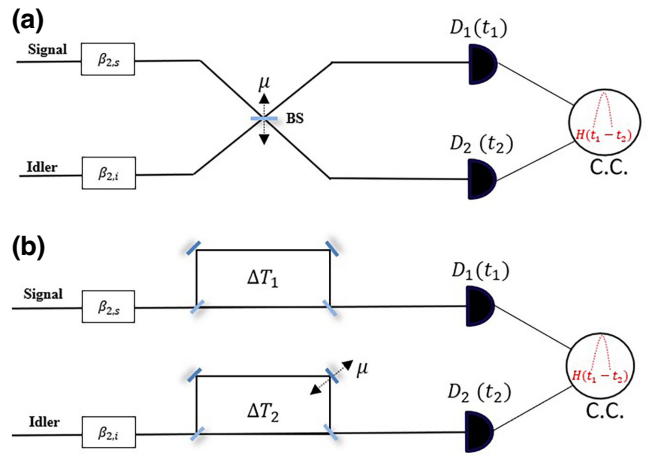


FIG. 1. (a) HOM interferometer and (b) Franson interferometer with dispersive media in the photon paths. BS, beam splitter; C.C., coincidence counter.

Considering the presence of dispersive media in both the signal path and the idler path, the dispersion experienced by the signal and idler photons around their center angular frequencies can be represented as $\beta_{2,s}$ and $\beta_{2,i}$, respectively. Then the expression for $a_{1(2)}(\omega)$ can be related to that of the input signal and idler photons by

$$\begin{aligned} \hat{a}_{1(2)}(\omega) &= \frac{1}{\sqrt{2}} (a_s(\omega) e^{i\beta_{2,s}(\omega - \omega_{s,0})^2} \\ &\quad \pm a_i(\omega) e^{i\beta_{2,i}(\omega - \omega_{i,0})^2} e^{i\omega\mu}), \end{aligned} \quad (3)$$

where μ represents the relative delay between the signal-photon and idler-photon paths in front of the 50:50 beam splitter. $\omega_{s,0}$ and $\omega_{i,0}$ denote the center angular frequencies of the signal and idler photons, respectively. Substituting Eq. (3) into Eq. (1), we can write the HOMI coincidence rate as

$$\begin{aligned} P_{c,\text{HOMI}} &\propto \int \int dt_1 dt_2 e^{-\frac{(t_1 - t_2)^2}{2\tau^2}} \int d\omega_1 \int d\omega_2 \int d\omega_3 \int d\omega_4 e^{-i\omega_1 t_1} e^{-i\omega_2 t_2} e^{i\omega_3 t_1} e^{i\omega_4 t_2} \\ &\times \langle \psi_{\text{in}} | (a_s^+(\omega_1) e^{-i\beta_{2,s}(\omega_1 - \omega_{s,0})^2} + a_i^+(\omega_1) e^{-i\beta_{2,i}(\omega_1 - \omega_{i,0})^2} e^{-i\omega_1 \mu}) \\ &\times (a_s^+(\omega_2) e^{-i\beta_{2,s}(\omega_2 - \omega_{s,0})^2} - a_i^+(\omega_2) e^{i\beta_{2,i}(\omega_2 - \omega_{i,0})^2} e^{-i\omega_2 \mu}) \\ &\times (a_s(\omega_3) e^{i\beta_{2,s}(\omega_3 - \omega_{s,0})^2} + a_i(\omega_3) e^{i\beta_{2,i}(\omega_3 - \omega_{i,0})^2} e^{i\omega_3 \mu}) \\ &\times (a_s(\omega_4) e^{i\beta_{2,s}(\omega_4 - \omega_{s,0})^2} - a_i(\omega_4) e^{i\beta_{2,i}(\omega_4 - \omega_{i,0})^2} e^{i\omega_4 \mu}) | \psi_{\text{in}} \rangle, \end{aligned} \quad (4)$$

where $|\psi_{\text{in}}\rangle$ is the Fourier transformation of $|\Psi_{\text{in}}\rangle$. For the two-photon state generated by the common SPDC process, $|\psi_{\text{in}}\rangle$ can be given by [29]

$$|\psi_{\text{in}}\rangle = \int d\tilde{\omega}_s d\tilde{\omega}_i \psi(\tilde{\omega}_s, \tilde{\omega}_i) \hat{a}_s^+(\tilde{\omega}_s) \hat{a}_i^+(\tilde{\omega}_i) |0\rangle, \quad (5)$$

where $|0\rangle$ represents the vacuum state and $\psi(\tilde{\omega}_s, \tilde{\omega}_i)$ is the spectral wave function of the generated biphoton source. This function is given by the product of the pump spectral function $\alpha(\tilde{\omega}_s, \tilde{\omega}_i)$ and the phase-matching function within the nonlinear crystal, denoted as $\phi(\tilde{\omega}_s, \tilde{\omega}_i)$. Here, $\tilde{\omega}_{s(i)}$ represents the angular frequency deviation of the signal (idler) photon from its center angular frequency $\omega_{s(i),0}$. It is important to note that $\omega_{s,0} + \omega_{i,0} = \omega_{p,0}$, where $\omega_{p,0}$ is the pump center angular frequency.

The spectral function of the quasimonochromatic light pump can be given by

$$\alpha(\tilde{\omega}_s, \tilde{\omega}_i) \propto \delta(\tilde{\omega}_s + \tilde{\omega}_i). \quad (6)$$

For a type-II nonlinear crystal with length L , the phase-matching function can be approximated by a Gaussian function as [30]

$$\phi(\tilde{\omega}_s, \tilde{\omega}_i) \propto e^{-aL^2(\gamma_s\tilde{\omega}_s + \gamma_i\tilde{\omega}_i)^2}, \quad (7)$$

where $a = 0.04822$ and $\gamma_{s(i)} \equiv k'_p(\omega_{p,0}) - k'_{s(i)}(\omega_{s(i),0})$, where k'_p , k'_s , and k'_i denote the first-order derivatives of the wave numbers for the pump, signal, and idler photons around their center frequencies, respectively. Assuming degenerate down-conversion, where $\omega_{s,0} = \omega_{i,0} = \omega_0$, the single-photon coherence width expressed as the FWHM can be given by $\Delta_0 = 2\sqrt{2\ln 2aL}|\gamma_s - \gamma_i|$. Substituting Eqs. (5)–(7) into Eq. (4), we can express the HOMI photon coincidence rate as follows:

$$P_{c,\text{HOMI}} \propto \int d\tilde{\omega}_1 \int d\tilde{\omega}_3 e^{-\frac{\tau^2(\tilde{\omega}_1 - \tilde{\omega}_3)^2}{2}} \\ \times e^{aL^2(\gamma_s - \gamma_i)^2(\tilde{\omega}_1^2 + \tilde{\omega}_3^2)} e^{-i(\beta_{2,s} + \beta_{2,i})(\tilde{\omega}_1^2 - \tilde{\omega}_3^2)} \\ \times (\cos[(\tilde{\omega}_1 - \tilde{\omega}_3)\mu] - \cos[(\tilde{\omega}_1 + \tilde{\omega}_3)\mu]). \quad (8)$$

Through deduction of Eq. (8), we obtain

$$P_{c,\text{HOMI}} \propto \frac{e^{-\frac{\mu^2}{aL^2(\gamma_s - \gamma_i)^2 + \tau^2 + \frac{(\beta_{2,s} + \beta_{2,i})^2}{aL^2(\gamma_s - \gamma_i)^2}}}}{\sqrt{aL^2(\gamma_s - \gamma_i)^2 + \tau^2 + \frac{(\beta_{2,s} + \beta_{2,i})^2}{aL^2(\gamma_s - \gamma_i)^2}}} \left(1 - \frac{\mu^2}{1 - e^{2aL^2(\gamma_s - \gamma_i)^2} \left(1 + \frac{aL^2(\gamma_s - \gamma_i)^2}{\tau^2} + \frac{(\beta_{2,s} + \beta_{2,i})^2}{\tau^2 aL^2(\gamma_s - \gamma_i)^2} \right)} \right). \quad (9)$$

Since the coincidence-measurement-window width is generally much larger than the single-photon coherence width, i.e., $\tau \gg \sqrt{aL}(\gamma_s - \gamma_i)$, the normalized HOMI coincidence rate as a function of the relative path delay between the signal and idler photons can be approximated as follows:

$$P_{c,\text{HOMI}}(\mu) \sim 1 - e^{-\frac{\mu^2}{2\left(aL^2(\gamma_s - \gamma_i)^2 + \frac{(\beta_{2,s} + \beta_{2,i})^2}{\tau^2}\right)}}. \quad (10)$$

Thus, energy-time entangled biphotons, after experiencing dispersion and temporal filtering, yield a broadened HOMI dip. The FWHM of this dip is given by

$$\Delta_{\text{HOMI}}(\tau) = 2\sqrt{2\ln 2aL}|\gamma_s - \gamma_i| \sqrt{1 + \frac{(\beta_{2,s} + \beta_{2,i})^2}{aL^2(\gamma_s - \gamma_i)^2 \tau^2}}. \quad (11)$$

As long as the temporal filtering is removed, or $\tau \gg |\beta_{2,s} + \beta_{2,i}|/\sqrt{aL}|\gamma_s - \gamma_i|$ is satisfied, $\Delta'_{\text{HOMI}} = \Delta_0 = 2\sqrt{2\ln 2aL}|\gamma_s - \gamma_i|$ is deduced, and the previously well-known dispersion cancellation characteristic of two-photon quantum interference [24–26] is recovered.

On the other hand, for the FI case [Fig. 1(b)], the expression for $\hat{a}_{1(2)}(\omega)$ at the output of the interferometer can be related to that of the input signal and idler photons by

$$\hat{a}_{1(2)}(\omega) = \frac{1}{2} \hat{a}_{s(i)}(\omega) e^{i\beta_{2,s(i)}(\omega - \omega_0)^2} (1 + e^{i\omega\Delta T_{1(2)}}), \quad (12)$$

where ΔT_1 and ΔT_2 respectively represent the transit time difference between the longer and shorter arms of the unbalanced Mach-Zehnder interferometers (UMZIs) in the signal and idler paths. Equation (1) can thus be rewritten as

$$P_{c,\text{FI}} \propto \int \int dt_1 dt_2 e^{-\frac{(t_1 - t_2)^2}{2\tau^2}} \int d\omega_1 \int d\omega_2 \int d\omega_3 \int d\omega_4 \langle \psi_{\text{in}} | a_s^\dagger(\omega_1) a_i^\dagger(\omega_2) a_s(\omega_3) a_i(\omega_4) e^{-i\omega_1 t_1} e^{-i\omega_2 t_2} e^{i\omega_3 t_1} e^{i\omega_4 t_2} \\ \times e^{-i\beta_{2,s}(\omega_1 - \omega_{s,0})^2} e^{-i\beta_{2,i}(\omega_2 - \omega_{i,0})^2} (1 + e^{i\omega_1 \Delta T_1}) (1 + e^{i\omega_2 \Delta T_2}) \\ \times e^{i\beta_{2,s}(\omega_3 - \omega_{s,0})^2} e^{i\beta_{2,i}(\omega_4 - \omega_{i,0})^2} (1 + e^{-i\omega_3 \Delta T_1}) (1 + e^{-i\omega_4 \Delta T_2}) | \psi_{\text{in}} \rangle. \quad (13)$$

Substituting Eqs. (5)–(7) into Eq. (13), we can obtain the photon coincidence rate as follows:

$$\begin{aligned} P_{c,\text{FI}} \propto & \int d\tilde{\omega}_1 \int d\tilde{\omega}_3 e^{-\frac{\tau^2(\tilde{\omega}_1-\tilde{\omega}_3)^2}{2}} \\ & \times e^{-al^2(\gamma_s-\gamma_i)^2(\tilde{\omega}_1^2+\tilde{\omega}_3^2)} e^{-i(\beta_{2,s}+\beta_{2,i})(\tilde{\omega}_1^2-\tilde{\omega}_3^2)} \\ & \times \left(1 + e^{i(\omega_0+\tilde{\omega}_1)\Delta T_1}\right) \left(1 + e^{i(\omega_0-\tilde{\omega}_1)\Delta T_2}\right) \\ & \times \left(1 + e^{-i(\omega_0+\tilde{\omega}_3)\Delta T_1}\right) \left(1 + e^{-i(\omega_0-\tilde{\omega}_3)\Delta T_2}\right). \quad (14) \end{aligned}$$

To ensure observation of only the two-photon Franson interferogram, it is necessary for $\Delta T_1 \approx \Delta T_2 \approx \Delta T \gg \sqrt{aL}(\gamma_s - \gamma_i)$ to be satisfied [28]. When incorporating this approximation into the deduction, we can express the normalized two-photon FI coincidence rate as follows (details can be found in the Appendix):

$$\begin{aligned} P_{c,\text{FI}}(\mu) \propto & 1 + e^{-\frac{\mu^2}{2\tau^2\left(1+\frac{(\beta_{2,s}+\beta_{2,i})^2}{al^2(\gamma_s-\gamma_i)^2\tau^2}\right)}} \\ & + 2e^{-\frac{\mu^2}{8al^2(\gamma_s-\gamma_i)^2\left(1+\left(\frac{\beta_{2,i}+\beta_{2,s}}{\sqrt{aL}(\gamma_s-\gamma_i)\tau}\right)^2\right)}} \\ & \times \cos(\omega_0(2\Delta T + \mu)) \\ & \sim 1 + e^{-\frac{\mu^2}{8al^2(\gamma_s-\gamma_i)^2\left(1+\left(\frac{\beta_{2,i}+\beta_{2,s}}{\sqrt{aL}(\gamma_s-\gamma_i)\tau}\right)^2\right)}} \\ & \times \cos(\omega_0(2\Delta T + \mu)), \quad (15) \end{aligned}$$

where $\mu = \Delta T_1 - \Delta T_2$ denotes the path difference between the two UMZIs. The FI graph displays a Gaussian-enveloped oscillation at frequency ω_0 with an envelope width given by

$$\Delta_{\text{FI}}(\tau) = 4\sqrt{2\ln 2aL}|\gamma_s - \gamma_i| \sqrt{1 + \frac{(\beta_{2,s} + \beta_{2,i})^2}{al^2(\gamma_s - \gamma_i)^2\tau^2}}. \quad (16)$$

By comparing Eqs. (11) and (16), we can see that the width of the FI fringe is exactly twice the HOMI width. In the case of $\tau \gg |\beta_{2,s} + \beta_{2,i}|/\sqrt{aL}|\gamma_s - \gamma_i|$, Eq. (16) can be reduced to $\Delta'_{\text{FI}} = 2\Delta_0 = 4\sqrt{2\ln 2aL}|\gamma_s - \gamma_i|$ and the nonlocal dispersion cancellation characteristic of the FI is recovered as well [18].

On the other hand, when strong temporal filtering is applied so that $\tau \ll |\beta_{2,s} + \beta_{2,i}|/\sqrt{aL}|\gamma_s - \gamma_i|$ is satisfied, the approximations of Eqs. (11) and (16) yield $\Delta''_{\text{FI}} = 2\Delta''_{\text{HOMI}} \approx 4\sqrt{2\ln 2}(|\beta_{2,s} + \beta_{2,i}|/\tau)$. Under this condition, by measuring the two-photon quantum interference width, one can evaluate the dispersion involved in the photon propagation paths. Since HOMI measurements need to

ensure spectral indistinguishability between signal and idler photons, the ability to characterize dispersion as a function of wavelength is significantly restricted. However, with the FI setup, the performance is no longer limited by the two-photon spectral indistinguishability. By changing the working temperature of the nonlinear medium for the SPDC, one can tune the center wavelengths of the down-converted biphotons in a quite large dynamic range [31,32]. In this case, the group delay dispersion (GDD) as a function of the wavelength of the dispersive medium involved can be easily measured. Through numerical derivatives, the higher-order dispersion properties of the dispersive medium involved can be derived simultaneously.

III. EXPERIMENTAL SETUP

On the basis of the theoretical model described above, both types of two-photon quantum interferometer were tested. The experimental setup is depicted in Fig. 2. The energy-time entangled photon-pair source was generated from a 10-mm-long piece of type-II Periodically Poled Lithium Niobate (PPLN) waveguide (HC Photonics Corp.), which was pumped by a continuous-wave distributed-Bragg-reflector laser (Photodigm Inc.) at 780 nm [33]. Under such a SPDC configuration, the single-photon coherence width Δ_0 was calculated to be approximately 1.48 ps. After filtering out of the residual pump beam, the signal and idler photons with orthogonal polarization were coupled into a fiber-optic polarization beam splitter (FPBS) and separated into two fiber paths marked as *s* and *i*, respectively, in Fig. 2.

To investigate the dispersion effect, fiber-Bragg-grating-(FBG-)based dispersion compensation modules (DCM-CB, Proximion AB), with their nominal GDD values 1545 nm being 165, 330, 495, and 825 ps/nm, respectively, and their length being about 12.25 m for each, were inserted into the idler path. In the experimental configuration of the HOM interferometer [Fig. 2(b)], it is crucial that the signal-photon path preceding the HOM interferometer maintains a length equivalent to that of the idler-photon path. As a result, extra single-mode fibers were introduced into the signal path to account for various FBG scenarios and to effectively counterbalance the delay caused by the FBGs. For the HOMI experimental scheme [Fig. 2(b)], an optical delay line (ODL; General Photonics Inc.) with a fixed delay of 100 ps was inserted in the signal path. The ODL was connected to the signal path by a single-mode fiber and a fiber coupler, while a motorized optical delay line (MDL-002, General Photonics Inc.), which is adjustable from 0 to 560 ps with a resolution of 1 fs, was placed in the idler path. Afterward, the signal and idler photons were fed into a 50:50 fiber-based beam splitter and detected by two superconducting nanowire single-photon detectors (SNSPDs Photec Ltd.), which contribute to a

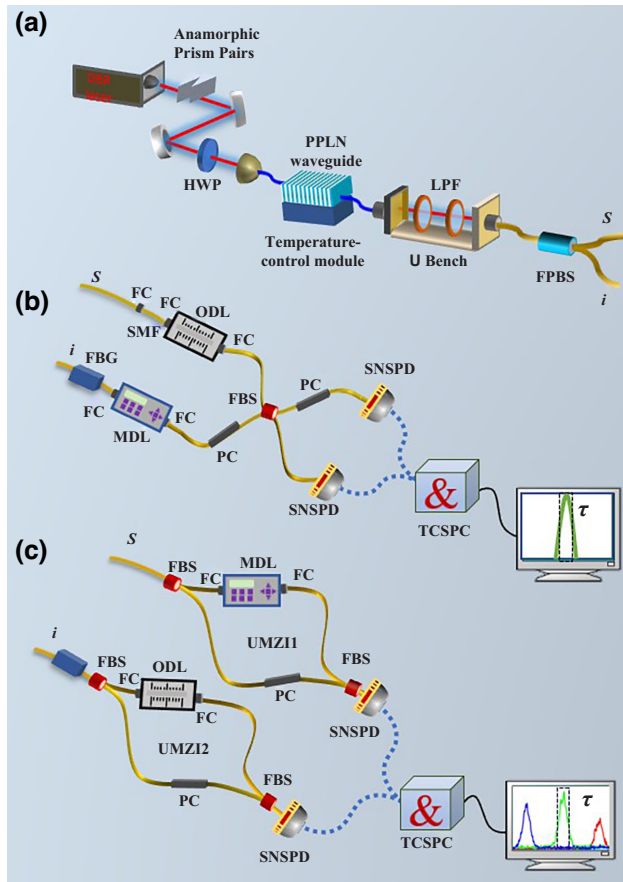


FIG. 2. Experimental setup for (a) the generation of an energy-time entangled biphoton source, (b) the HOM interferometer, and (c) the Franson interferometer. The energy-time entangled photon pairs are generated by a continuous-wave-pumped SPDC. They are separated by the fiber-optic polarization beam splitter (FPBS) into two fiber paths: signal (*s*) and idler (*i*). After being transmitted through the dispersive module, they are routed to the respective interferometers. FBG, fiber Bragg grating; FBS, fiber-based beam splitter; FC, fiber coupler; HWP, half-wave plate; LPF, long-pass filter; MDL, motorized optical delay line; ODL, optical delay line; PC, polarization controller; PPLN, Periodically Poled Lithium Niobate waveguide; SMF, single-mode fiber; SNSPD, superconducting nanowire single-photon detector; TCSPC, time-correlated single-photon counter; UMZI, unbalanced Mach-Zehnder interferometer.

time jitter of about 65 ps as the FWHM. Two polarization controllers were used to adjust the polarization of the propagated photons. The detection events from the SNSPDs were connected to a time-correlated single-photon counting module (PicoHarp 300, PicoQuant) for coincidence measurement. The timing resolution was set at 4 ps during the measurement. By applying postselection on the coincidence-window width, we implemented temporal filtering. The FI experimental setup is shown in Fig. 2(c). All the experimental settings were kept the same, except that the interferometer was changed to the

FI type. Specifically, two unbalanced Mach-Zehnder interferometers (UMZI1 and UMZI2) were connected to the signal and idler paths, respectively. The motorized optical delay line was inserted in the long arm of UMZI1, while the ODL was placed in that of UMZI2, with the imbalances of the two UMZIs maintained almost identical ($\Delta T_1 \approx \Delta T_2$). To ensure accurate Franson-type quantum interference measurements, it is crucial to keep the path-delay differences within the two UMZIs nearly equivalent. In our experiment, we enclosed all UMZI components within a container to passively mitigate temperature fluctuations and vibrations, effectively maintaining both UMZIs' imbalances at approximately 500 ps. To further increase stability, optimizing the compactness of the UMZI configuration and improving isolation from the environment will be beneficial.

IV. EXPERIMENTAL RESULTS AND ANALYSIS

A. Dispersion-broadened HOMI dip width under temporal filtering

The two-photon HOM interference was first measured. Two experiments were conducted: one measured the HOMI width by varying the GDD in the idler path and keeping the coincidence window width fixed at 800 ps, while the other measured the HOMI width by varying the coincidence window width and keeping the GDD in

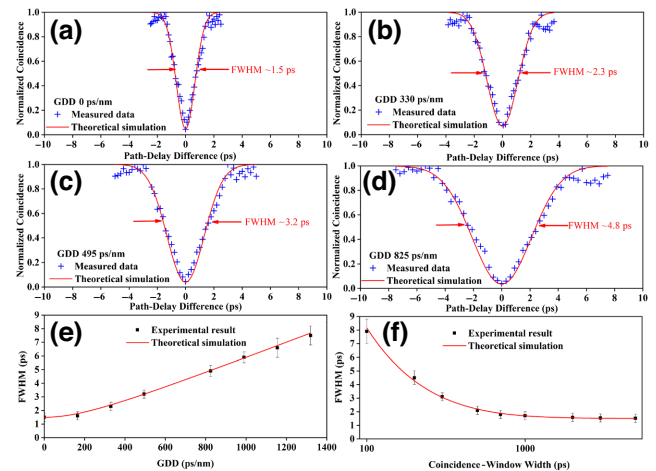


FIG. 3. Experimental results for the HOM interference measurement. For the coincidence window width fixed at 800 ps, (a)–(d) show the measured HOMI dip plots as a function of the path-delay difference between the signal and idler photons, with the GDD of the dispersive module in the idler-photon path being 0, 330, 495, and 825 ps/nm, respectively. (e) Measured FWHM HOMI dip width as a function of the GDD (black squares) and corresponding theoretical simulation (solid red curve). (f) Measured FWHM HOMI dip width for different coincidence window widths (black squares) and corresponding theoretical simulations (solid red curve) obtained with the GDD fixed at 165 ps/nm.

the idler path fixed at 165 ps/nm. The results are shown in Fig. 3.

By fixing the coincidence window width at 800 ps, Figs. 3(a)–3(d) show the measured HOMI-type dip fringes as a function of the path-delay difference between the signal and idler photons with the GDD of the dispersive module in the idler-photon path being 0, 330, 495, and 825 ps/nm, respectively. It can be seen that when no dispersion is inserted in the photon propagation path, the HOMI dip width is given by the single-photon coherence width of the biphoton source. With increase of the dispersion in the idler-photon path, the measured HOMI width increases accordingly. The measured HOMI dip width as a function of the GDD is plotted in Fig. 3(e) as black squares. The corresponding theoretical simulation curve based on Eq. (11) and the experimental parameters is also given in Fig. 3(e), and good agreement was achieved. Meanwhile, the measured FWHM HOMI dip width for different coincidence window widths obtained by fixing the GDD at 165 ps/nm (black squares) is plotted in Fig. 3(f), and the corresponding theoretical simulation (solid red curve) gives a simulated GDD of 172 ± 2.8 ps/nm, which is also consistent with the measured value of the FBG module in another experiment [34].

B. Dispersion-broadened FI fringe width under temporal filtering

Under the same experimental configurations, the two-photon Franson interference was also measured and is displayed in Fig. 4. For the coincidence window width fixed at 800 ps, the measured FI fringes as a function of the path-delay difference between the two UMZIs for different GDD cases are shown in Figs. 4(a)–4(d). As shown in Fig. 4(a), when no dispersion is inserted into the photon propagation path, the FI fringe width is twice the single-photon coherence width of the biphoton source. With increase of the dispersion in the idler-photon path, the measured FI fringe width experienced an increase with the same slope as that of the HOMI dip width. The measured FWHM FI fringe width as a function of the GDD is plotted in Fig. 4(e) as black squares. For the GDD fixed at 165 ps/nm, the measured FI fringe width for different coincidence window widths (black squares) is plotted in Fig. 4(f). On the basis of Eq. (16) and the experimental parameters, corresponding theoretical simulations for both results in Figs. 4(e) and 4(f) were also performed and are given by the solid red curves. The simulated GDD from Fig. 4(f) gives a value of 161 ± 2.6 ps/nm. One may notice that this value is different from that deduced from the HOMI measurement result. We think such a difference should be due to the instability of the UMZIs involved in the FI setup, which can also be observed from the irregularity of the contour in Figs. 4(a)–4(d). By packing the UMZIs into enclosures and applying temperature stabilization, an increase in the measurement precision can be expected.

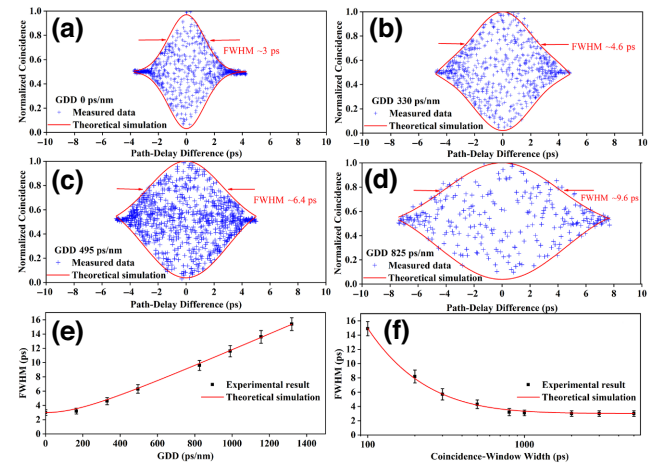


FIG. 4. Experimental results for the Franson interference measurement. For the coincidence window width fixed at 800 ps, (a)–(d) show the measured FI fringe plots as a function of the path-delay difference between the signal and idler photons with the GDD of the dispersive module in the idler-photon path being 0, 330, 495, and 825 ps/nm, respectively. (e) Measured FWHM FI fringe widths versus the GDD (black squares) and the corresponding theoretical simulation (solid red curve). (f) Measured FWHM FI fringe widths for different coincidence window widths obtained with the GDD fixed at 165 ps/nm (black squares) and the corresponding theoretical simulation (solid red curve).

The agreement between the theoretical simulations and the experimental results, as depicted in Figs. 3(f) and 4(f), effectively validates the utility of quantum interference measurements using temporal filtering as an effective means of characterizing chromatic dispersion. Given the flexibility of adjusting the temporal filtering through a postselection process on the coincidence window width, there is no need for additional instruments during the measurements. Moreover, the FI measurement is no longer constrained by local coincidence detection and spectral indistinguishability between the signal and idler photons, leading to a substantial improvement in its ability to characterize the wavelength-dependent dispersion properties of the dispersive media studied.

V. CONCLUSION

Quantum interference lies at the heart of many quantum optical phenomena and applications, including quantum information processing, quantum communication, and quantum sensing. Understanding the factors that influence the width of quantum interference patterns is essential for optimizing the performance of such systems. Temporal filtering is commonly used in practical quantum experiments for improving the interference visibility. However, it may introduce nontrivial side effects, especially when large dispersion is involved in the photon propagation paths. In this paper, we demonstrate both theoretically

and experimentally the dispersion broadening of the two-photon quantum interference width due to temporal filtering. This work enriches research on HOM-type and Franson-type quantum interferometry and holds significant value for advancing new quantum interference applications. Furthermore, such phenomenon can be used to characterize the dispersion properties of an unknown dispersive medium. This implementation offers a convenient dispersion measurement method by allowing flexible adjustment of the temporal-filtering width through postselection. Furthermore, the FI-based quantum interferometry surmounts the constraints posed by local coincidence measurements and the spectral indistinguishability of two photons, which is typical in HOM-based interferometry. This advantage significantly enhances its adaptability in assessing the wavelength-dependent dispersion characteristics of dispersive media. It is noteworthy that temporal filtering does

impact effective coincidence detection efficiency, necessitating sufficient measurement time for the effective SNR, especially when one is evaluating dispersive media with notable attenuation.

ACKNOWLEDGMENTS

This work was supported by the National Natural Science Foundation of China (Grants No. 12033007, No. 61801458, No. 12103058, No. 12203058, No. 12074309, and No. 61875205), the Youth Innovation Promotion Association, Chinese Academy of Sciences (Grants No. 2022413 and No. 2021408), the Western Young Scholar Project of the Chinese Academy of Sciences (Grants No. XAB2019B17 and No. XAB2019B15), and the China Postdoctoral Science Foundation (Grant No. 2022M723174).

APPENDIX: THEORETICAL DEDUCTION FOR THE FI COINCIDENCE RATE

In this appendix, we present the detailed deduction of Eq. (15), which describes the normalized photon coincidence rate at the output of the FI. Starting from Eq. (13), the substitution of Eqs. (5)–(7) leads to the expression of the rate as

$$\begin{aligned} P_{c,\text{FI}} &\propto \int \int dt_1 dt_2 e^{-\frac{(t_1-t_2)^2}{2\tau^2}} e^{-i(\tilde{\omega}_1-\tilde{\omega}_3)(t_1-t_2)} \int \int d\tilde{\omega}_1 d\tilde{\omega}_3 e^{-aL^2(\gamma_s-\gamma_i)^2(\tilde{\omega}_1^2+\tilde{\omega}_3^2)} e^{-i(\beta_{2,s}+\beta_{2,i})(\tilde{\omega}_1^2-\tilde{\omega}_3^2)} \\ &\quad \times \left(1 + e^{i(\omega_0+\tilde{\omega}_1)\Delta T_1}\right) \left(1 + e^{i(\omega_0-\tilde{\omega}_1)\Delta T_2}\right) \left(1 + e^{-i(\omega_0+\tilde{\omega}_3)\Delta T_1}\right) \left(1 + e^{-i(\omega_0-\tilde{\omega}_3)\Delta T_2}\right) \\ &\propto \int d\tilde{\omega}_1 \int d\tilde{\omega}_3 e^{-\frac{\tau^2(\tilde{\omega}_1-\tilde{\omega}_3)^2}{2}} e^{-aL^2(\gamma_s-\gamma_i)^2(\tilde{\omega}_1^2+\tilde{\omega}_3^2)} e^{-i(\beta_{2,s}+\beta_{2,i})(\tilde{\omega}_1^2-\tilde{\omega}_3^2)} \\ &\quad \times \left(1 + e^{i(\omega_0+\tilde{\omega}_1)\Delta T_1}\right) \left(1 + e^{-i(\omega_0+\tilde{\omega}_3)\Delta T_1}\right) \left(1 + e^{i(\omega_0-\tilde{\omega}_1)\Delta T_2}\right) \left(1 + e^{-i(\omega_0-\tilde{\omega}_3)\Delta T_2}\right). \end{aligned} \quad (\text{A1})$$

Expansion of the product terms of Eq. (A1) leads to the following expression:

$$\begin{aligned} P_{c,\text{FI}} &\propto \int \int d\tilde{\omega}_1 d\tilde{\omega}_3 e^{-\frac{\tau^2(\tilde{\omega}_1-\tilde{\omega}_3)^2}{2}} e^{-aL^2(\gamma_s-\gamma_i)^2(\tilde{\omega}_1^2+\tilde{\omega}_3^2)} e^{-i(\beta_{2,s}+\beta_{2,i})(\tilde{\omega}_1^2-\tilde{\omega}_3^2)} (1 + e^{i(\omega_0+\tilde{\omega}_1)\Delta T_1} + e^{-i(\omega_0+\tilde{\omega}_3)\Delta T_1} + e^{i(\tilde{\omega}_1-\tilde{\omega}_3)\Delta T_1} \\ &\quad + e^{i(\omega_0-\tilde{\omega}_1)\Delta T_2} + e^{-i(\omega_0-\tilde{\omega}_3)\Delta T_2} + e^{-i(\tilde{\omega}_1-\tilde{\omega}_3)\Delta T_2} + e^{i\omega_0(\Delta T_1+\Delta T_2)+i\tilde{\omega}_1(\Delta T_1-\Delta T_2)} + e^{i\omega_0(\Delta T_1-\Delta T_2)+i\tilde{\omega}_1\Delta T_1+i\tilde{\omega}_3\Delta T_2} \\ &\quad + e^{i(\omega_0+\tilde{\omega}_1)\Delta T_1-i(\tilde{\omega}_1-\tilde{\omega}_3)\Delta T_2} + e^{-i\omega_0(\Delta T_1+\Delta T_2)-i\tilde{\omega}_3(\Delta T_1-\Delta T_2)} + e^{-i(\omega_0+\tilde{\omega}_3)\Delta T_1-i(\tilde{\omega}_1-\tilde{\omega}_3)\Delta T_2} + e^{i(\omega_0-\tilde{\omega}_1)\Delta T_2+i(\tilde{\omega}_1-\tilde{\omega}_3)\Delta T_1} \\ &\quad + e^{-i(\omega_0-\tilde{\omega}_3)\Delta T_2+i(\tilde{\omega}_1-\tilde{\omega}_3)\Delta T_1} + e^{i(\tilde{\omega}_1-\tilde{\omega}_3)(\Delta T_1-\Delta T_2)}). \end{aligned} \quad (\text{A2})$$

Because of symmetry, the exchange between $\tilde{\omega}_1$ and $\tilde{\omega}_3$ does not affect the integration. Therefore, Eq. (A2) can be rewritten as

$$\begin{aligned} P_{c,\text{FI}} &\propto \int \int d\tilde{\omega}_1 d\tilde{\omega}_3 e^{-\frac{\tau^2(\tilde{\omega}_1-\tilde{\omega}_3)^2}{2}} e^{-aL^2(\gamma_s-\gamma_i)^2(\tilde{\omega}_1^2+\tilde{\omega}_3^2)} e^{-i(\beta_{2,s}+\beta_{2,i})(\tilde{\omega}_1^2-\tilde{\omega}_3^2)} (1 + e^{i(\omega_0+\tilde{\omega}_1)\Delta T_1} + e^{-i(\omega_0+\tilde{\omega}_1)\Delta T_1} + e^{i(\omega_0-\tilde{\omega}_1)\Delta T_2} \\ &\quad + e^{-i(\omega_0-\tilde{\omega}_1)\Delta T_2} + e^{i\omega_0(\Delta T_1+\Delta T_2)+i\tilde{\omega}_1(\Delta T_1-\Delta T_2)} + e^{-i\omega_0(\Delta T_1+\Delta T_2)-i\tilde{\omega}_1(\Delta T_1-\Delta T_2)} + e^{i\omega_0(\Delta T_1-\Delta T_2)+i\tilde{\omega}_1\Delta T_1+i\tilde{\omega}_3\Delta T_2} \\ &\quad + e^{-i\omega_0(\Delta T_1-\Delta T_2)-i\tilde{\omega}_1\Delta T_1-i\tilde{\omega}_3\Delta T_2} + e^{i(\omega_0+\tilde{\omega}_1)\Delta T_1-i(\tilde{\omega}_1-\tilde{\omega}_3)\Delta T_2} + e^{-i(\omega_0+\tilde{\omega}_1)\Delta T_1+i(\tilde{\omega}_1-\tilde{\omega}_3)\Delta T_2} \\ &\quad + e^{i(\omega_0-\tilde{\omega}_1)\Delta T_2+i(\tilde{\omega}_1-\tilde{\omega}_3)\Delta T_1} + e^{-i(\omega_0-\tilde{\omega}_1)\Delta T_2-i(\tilde{\omega}_1-\tilde{\omega}_3)\Delta T_1} + e^{i(\tilde{\omega}_1-\tilde{\omega}_3)\Delta T_1} + e^{-i(\tilde{\omega}_1-\tilde{\omega}_3)\Delta T_2} + e^{i(\tilde{\omega}_1-\tilde{\omega}_3)(\Delta T_1-\Delta T_2)}). \end{aligned} \quad (\text{A3})$$

Let $\tilde{\omega}_1 - \tilde{\omega}_3 = x$, $\tilde{\omega}_1 + \tilde{\omega}_3 = y$. Equation (A3) can then be transformed to

$$\begin{aligned} P_{c,\text{FI}} \propto & \int dxdye^{-\frac{\tau^2x^2}{2}}e^{-\frac{aL^2(\gamma_s-\gamma_i)^2}{2}(x^2+y^2)}e^{-i(\beta_{2,s}+\beta_{2,i})xy}(1+e^{i(\omega_0+\frac{x+y}{2})\Delta T_1}+e^{-i(\omega_0+\frac{x+y}{2})\Delta T_1}+e^{i(\omega_0-\frac{x+y}{2})\Delta T_2} \\ & +e^{-i(\omega_0-\frac{x+y}{2})\Delta T_2}+e^{i\omega_0(\Delta T_1+\Delta T_2)+i\frac{x+y}{2}(\Delta T_1-\Delta T_2)}+e^{-i\omega_0(\Delta T_1+\Delta T_2)-i\frac{x+y}{2}(\Delta T_1-\Delta T_2)}+e^{i\omega_0(\Delta T_1-\Delta T_2)+i\frac{x+y}{2}\Delta T_1+i\frac{x-y}{2}\Delta T_2} \\ & +e^{-i\omega_0(\Delta T_1-\Delta T_2)-i\frac{x+y}{2}\Delta T_1-i\frac{x-y}{2}\Delta T_2}+e^{i(\omega_0+\frac{x+y}{2})\Delta T_1-ix\Delta T_2}+e^{-i(\omega_0+\frac{x+y}{2})\Delta T_1+ix\Delta T_2}+e^{i(\omega_0-\frac{x+y}{2})\Delta T_2+ix\Delta T_1} \\ & +e^{-i(\omega_0-\frac{x+y}{2})\Delta T_2-ix\Delta T_1}+e^{ix\Delta T_1}+e^{-ix\Delta T_2}+e^{ix(\Delta T_1-\Delta T_2)}). \end{aligned} \quad (\text{A4})$$

To simplify the integral calculation, $A = \tau^2$, $B = aL^2(\gamma_s - \gamma_i)^2$, and $\beta = \beta_{2,s} + \beta_{2,i}$ are defined, and Eq. (A4) is transformed to

$$\begin{aligned} P_{c,\text{FI}} \propto & 1 + e^{-\frac{B\Delta T_1^2}{2(AB+B^2+\beta^2)}} + e^{-\frac{B\Delta T_2^2}{2(AB+B^2+\beta^2)}} + e^{-\frac{B(\Delta T_1-\Delta T_2)^2}{2(AB+B^2+\beta^2)}} + 2e^{-\frac{\Delta T_1^2(A+2B)}{8(AB+B^2+\beta^2)}} \cos\left(\omega_0\Delta T_1 + \frac{2\beta\Delta T_1^2}{8(AB+B^2+\beta^2)}\right) \\ & + e^{-\frac{\Delta T_2^2(A+2B)}{8(AB+B^2+\beta^2)}} \cos\left(\omega_0\Delta T_2 - \frac{2\beta\Delta T_2^2}{8(AB+B^2+\beta^2)}\right) \\ & + 2e^{-\frac{(\Delta T_1-\Delta T_2)^2(A+2B)}{8(AB+B^2+\beta^2)}} \cos\left(\omega_0(\Delta T_1 + \Delta T_2) + \frac{2\beta(\Delta T_1 - \Delta T_2)^2}{8(AB+B^2+\beta^2)}\right) \\ & + 2e^{-\frac{B(\Delta T_1^2+\Delta T_2^2)+A\Delta T_1^2}{8(B(A+B)+\beta^2)}} \cos\left(\omega_0(\Delta T_1 - \Delta T_2) + \frac{2\beta\Delta T_1\Delta T_2}{8(AB+B^2+\beta^2)}\right) \\ & + 2e^{-\frac{A\Delta T_1^2+2B(\Delta T_1^2-2\Delta T_1\Delta T_2+2\Delta T_2^2)}{8(AB+B^2+\beta^2)}} \cos\left(\omega_0\Delta T_1 + \frac{2\beta\Delta T_1(\Delta T_1 - 2\Delta T_2)}{8(AB+B^2+\beta^2)}\right) \\ & + 2e^{-\frac{A\Delta T_2^2+2B(\Delta T_2^2-2\Delta T_1\Delta T_2+2\Delta T_1^2)}{8(AB+B^2+\beta^2)}} \cos\left(\omega_0\Delta T_2 + \frac{2\beta\Delta T_2(\Delta T_2 - 2\Delta T_1)}{8(AB+B^2+\beta^2)}\right). \end{aligned} \quad (\text{A5})$$

Since $\Delta T_1 \approx \Delta T_2 \gg \sqrt{aL}(\gamma_s - \gamma_i)$ is satisfied, Eq. (A5) can be approximated to

$$P_{c,\text{FI}} \propto 1 + e^{-\frac{B(\Delta T_1-\Delta T_2)^2}{2(AB+B^2+\beta^2)}} + 2e^{-\frac{(\Delta T_1-\Delta T_2)^2(A+2B)}{8(AB+B^2+\beta^2)}} \cos\left(\omega_0(\Delta T_1 + \Delta T_2) + \frac{2\beta(\Delta T_1 - \Delta T_2)^2}{8(AB+B^2+\beta^2)}\right). \quad (\text{A6})$$

Consider that

$$\begin{aligned} AB + B^2 + \beta^2 &= aL^2(\gamma_s - \gamma_i)^2 \left(\tau^2 + aL^2(\gamma_s - \gamma_i)^2 + \left(\frac{\beta_{2,i} + \beta_{2,s}}{\sqrt{aL}(\gamma_s - \gamma_i)} \right)^2 \right), \\ A + 2B &= \tau^2 + 2aL^2(\gamma_s - \gamma_i)^2. \end{aligned} \quad (\text{A7})$$

As long as $\tau^2 \gg aL^2(\gamma_s - \gamma_i)^2$, Eq. (A7) can be deduced that

$$\begin{aligned} \frac{8(AB+B^2+\beta^2)}{A+2B} &\approx 8aL^2(\gamma_s - \gamma_i)^2 \left(1 + \frac{aL^2(\gamma_s - \gamma_i)^2}{\tau^2} + \left(\frac{\beta_{2,i} + \beta_{2,s}}{\sqrt{aL}(\gamma_s - \gamma_i)\tau} \right)^2 \right) \\ &\approx 8aL^2(\gamma_s - \gamma_i)^2 \left(1 + \left(\frac{\beta_{2,i} + \beta_{2,s}}{\sqrt{aL}(\gamma_s - \gamma_i)\tau} \right)^2 \right). \end{aligned} \quad (\text{A8})$$

Assume that $\Delta T_1 \approx \Delta T_2 \approx \Delta T$ and $\Delta T_1 - \Delta T_2 = \mu$. The coincidence rate for the FI is thus reduced to

$$P_{c,\text{FI}} \propto 1 + e^{-\frac{\mu^2}{2\tau^2 \left(1 + \frac{aL^2(\gamma_s - \gamma_i)^2}{\tau^2} + \left(\frac{\beta_{2,i} + \beta_{2,s}}{\sqrt{aL}(\gamma_s - \gamma_i)\tau}\right)^2\right)}} + 2e^{-\frac{\mu^2}{8aL^2(\gamma_s - \gamma_i)^2 \left(1 + \frac{aL^2(\gamma_s - \gamma_i)^2}{\tau^2} + \left(\frac{\beta_{2,i} + \beta_{2,s}}{\sqrt{aL}(\gamma_s - \gamma_i)\tau}\right)^2\right)}} \cos(\omega_0(2\Delta T + \mu)). \quad (\text{A9})$$

When $\mu^2/8aL^2(\gamma_s - \gamma_i)^2 \left\{ 1 + [(\beta_{2,i} + \beta_{2,s})/\sqrt{aL}(\gamma_s - \gamma_i)\tau]^2 \right\} \ll 0$ is satisfied, Eq. (15) is obtained.

- [1] C. K. Hong, Z. Y. Ou, and L. Mandel, Measurement of subpicosecond time intervals between two photons by interference, *Phys. Rev. Lett.* **59**, 2044 (1987).
- [2] Y. L. Zhao, T. Yang, Y. Tong, J. Wang, J. H. Luan, Z. B. Jiao, D. Chen, Y. Yang, A. Hu, C. T. Liu, and J. J. Kai, Heterogeneous precipitation behavior and stacking-fault-mediated deformation in a CoCrNi-based medium-entropy alloy, *Acta. Mater.* **138**, 72 (2017).
- [3] J. Pan, Z. Chen, C. Lu, H. Weinfurter, A. Zeilinger, and M. Żukowski, Multiphoton entanglement and interferometry, *Rev. Mod. Phys.* **84**, 777 (2012).
- [4] J. Pan, B. Dik, W. Harald, and Z. Anton, Experimental entanglement swapping: Entangling photons that never interacted, *Phys. Rev. Lett.* **80**, 3891 (1998).
- [5] S. Carrasco, J. P. Torres, L. Torner, A. Sergienko, B. E. A. Saleh, and M. C. Teich, Enhancing the axial resolution of quantum optical coherence tomography by chirped quasi-phase matching, *Opt. Lett.* **29**, 2429 (2004).
- [6] R. Quan, Y. Zhai, M. Wang, T. Liu, S. Zhang, and R. Dong, Demonstration of quantum synchronization based on second-order quantum coherence of entangled photons, *Sci. Rep.* **6**, 2429 (2016).
- [7] X. Ma, S. Zotter, J. Kofler, R. Ursin, T. Jennewein, Č. Brukner, and A. Zeilinger, Experimental delayed-choice entanglement swapping, *Nat. Phys.* **8**, 479 (2012).
- [8] R. Quan, R. Dong, Y. Zhai, F. Hou, X. Xiang, Z. Hui, C. Lv, Z. Wang, L. You, T. Liu, S. Zhang, and R. Dong, Simulation and realization of a second-order quantum-interference-based quantum clock synchronization at the femtosecond level, *Opt. Lett.* **44**, 614 (2019).
- [9] L. Schwarz and S. van Enk, Detecting the drift of quantum sources: Not the de Finetti theorem, *Phys. Rev. Lett.* **106**, 180501 (2011).
- [10] R. Jozsa, D. S. Abrams, J. P. Dowling, and C. P. Williams, Quantum clock synchronization based on shared prior entanglement, *Phys. Rev. Lett.* **85**, 2010 (2000).
- [11] C. Lang, C. Eichler, L. Steffen, J. M. Fink, M. J. Woolley, A. Blais, and A. Wallraff, Correlations, indistinguishability and entanglement in Hong-Ou-Mandel experiments at microwave frequencies, *Nat. Phys.* **9**, 345 (2013).
- [12] H. Jin, F. M. Liu, P. Xu, J. L. Xia, M. L. Zhong, Y. Yuan, J. W. Zhou, Y. X. Gong, W. Wang, and S. N. Zhu, On-chip generation and manipulation of entangled photons based on reconfigurable lithium-niobate waveguide circuits, *Phys. Rev. Lett.* **113**, 103601 (2014).
- [13] T. E. Northup and R. Blatt, Quantum information transfer using photons, *Nat. Photonics* **8**, 356 (2014).

- [14] K. Toyoda, R. Hiji, A. Noguchi, and S. Urabe, Hong-Ou-Mandel interference of two phonons in trapped ions, *Nature* **527**, 74 (2015).
- [15] C. Xiong, X. Zhang, Z. Liu, M. J. Collins, A. Mahendra, L. Helt, M. J. Steel, D.-Y. Choi, C. Chae, and P. Leong, Active temporal multiplexing of indistinguishable heralded single photons, *Nat. Commun.* **7**, 10853 (2016).
- [16] J. D. Franson, Bell inequality for position and time, *Phys. Rev. Lett.* **62**, 2205 (1989).
- [17] J. Park, H. Kim, and H. S. Moon, Indistinguishability of temporally separated pairwise two-photon state of thermal photons in Franson-type interferometry, *Sci. Rep.* **12**, 5456 (2022).
- [18] H. Kim, S. M. Lee, O. Kwon, and H. S. Moon, Two-photon interference of polarization-entangled photons in a Franson interferometer, *Sci. Rep.* **7**, 5772 (2017).
- [19] F. Bouchard, A. Sit, Y. Zhang, R. Fickler, F. M. Miatto, Y. Yao, F. Sciarrino, and E. Karimi, Two-photon interference: The Hong-Ou-Mandel effect, *Rep. Prog. Phys.* **84**, 012402 (2020).
- [20] J. F. Clauser, M. A. Horne, A. Shimony, and R. A. Holt, Proposed experiment to test local hidden-variable theories, *Phys. Rev. Lett.* **23**, 880 (1969).
- [21] Z. Zhang, J. Mower, D. Englund, F. N. Wong, and J. H. Shapiro, Unconditional security of time-energy entanglement quantum key distribution using dual-basis interferometry, *Phys. Rev. Lett.* **112**, 120506 (2014).
- [22] E. Y. Zhu, C. Corbari, A. V. Gladyshev, P. G. Kazansky, and L. Qian, Franson interferometry with a single pulse, *Front. Optoelectron.* **11**, 148 (2018).
- [23] X. You, M. Zheng, S. Chen, R. Liu, J. Qin, M. Xu, Z. Ge, T. Chung, Y. Qiao, and Y. Jiang, Quantum interference with independent single-photon sources over 300 km fiber, *Adv. Photonics* **4**, 066003 (2022).
- [24] A. Steinberg, P. Kwiat, and R. Chiao, Dispersion cancellation in a measurement of the single-photon propagation velocity in glass, *Phys. Rev. Lett.* **68**, 2421 (1992).
- [25] M. B. Nasr, B. E. Saleh, A. V. Sergienko, and M. C. Teich, Demonstration of dispersion-canceled quantum-optical coherence tomography, *Phys. Rev. Lett.* **91**, 083601 (2003).
- [26] J. Ryu, K. Cho, C.-H. Oh, and H. Kang, All-order dispersion cancellation and energy-time entangled state, *Opt. Express* **25**, 1360 (2017).
- [27] R. Ursin, F. Tiefenbacher, T. Schmitt-Manderbach, H. Weier, T. Scheidl, M. Lindenthal, B. Blauensteiner, T. Jennewein, J. Perdigues, and P. Trojek, Entanglement-based quantum communication over 144 km, *Nat. Phys.* **3**, 481 (2007).
- [28] B. Korzh, C. C. W. Lim, R. Houlmann, N. Gisin, M. J. Li, D. Nolan, B. Sanguinetti, R. Thew, and H. Zbinden,

- Provably secure and practical quantum key distribution over 307 km of optical fibre, [Nat. Photonics](#) **9**, 163 (2015).
- [29] V. Giovannetti, L. Maccone, J. H. Shapiro, and F. Wong, Extended phase-matching conditions for improved entanglement generation, [Phys. Rev. A](#) **66**, 43813 (2002).
- [30] F. Hou, R. Quan, R. Dong, X. Xiang, B. Li, T. Liu, X. Yang, H. Li, L. You, and Z. Wang, Fiber-optic two-way quantum time transfer with frequency-entangled pulses, [Phys. Rev. A](#) **100**, 023849 (2019).
- [31] X. Xiang, R. Quan, Y. Liu, B. Shi, H. Hong, Y. Jin, T. Liu, R. Dong, and S. Zhang, Widely flexible and finely adjustable nonlocal dispersion cancellation with wavelength tuning, [Opt. Express](#) **30**, 44487 (2022).
- [32] B. Li, Z. Xia, X. Xiang, Y. Jin, R. Quan, R. Dong, T. Liu, and S. Zhang, Experimental method for fast measuring the phase-matched wavelengths of entangled photons by wavelength-to-time mapping, [Chin. J. Lasers](#) **48**, 0312001 (2021).
- [33] X. Xiang, R. Dong, R. Quan, Y. Jin, Y. Yang, M. Li, T. Liu, and S. Zhang, Hybrid frequency-time spectrograph for the spectral measurement of the two-photon state, [Opt. Lett.](#) **45**, 2993 (2020).
- [34] Y. Jin, Y. Yang, H. Hong, X. Xiang, R. Quan, T. Liu, N. Zhu, M. Li, R. Dong, and S. Zhang, Surpassing the classical limit of microwave photonic frequency fading effect by quantum microwave photonics, [Photonics Res.](#) **11**, 1094 (2023).